ACS APPLIED MATERIALS & INTERFACES

www.acsami.org

Research Article

# Study of a High-Voltage NMC Interphase in the Presence of a Thiophene Additive Realized by Operando SHINERS

Felix Pfeiffer, Diddo Diddens, Matthias Weiling, and Masoud Baghernejad*

Cite This: ACS Appl. Mater. Interfaces 2023, 15, 6676−6686

Read Online

ACCESS | Metrics & More | Article Recommendations | Supporting Information

**ABSTRACT:** Improving the electrochemical properties and cycle life of high-voltage cathodes in lithium-ion batteries requires a deep understanding of the structural properties and failure mechanisms at the cathode electrolyte interphase (CEI). We present a study implementing an advanced Raman spectroscopy technique to specifically address the compositional features of interphase during cell operation. Our operando technique, shell-isolated nanoparticle-enhanced Raman spectroscopy (SHINERS), provides a reliable platform to investigate the dynamics of the interphase structure and elucidate the compositional changes near the cathode surface. To improve the CEI properties, thiophene was introduced and investigated as an effective, high-voltage film-forming additive by largely diminishing the capacity fading triggered at high potentials in $LiNi_{1/3}Co_{1/3}Mn_{1/3}O_2$ cathodes. While the cells without thiophene show severe capacity fading, cells with an optimized concentration of thiophene exhibit a significant performance improvement. Operando SHINERS detects the presence of a stable CEI. The results suggest that the composition of the CEI is dominated by polythiophene and copolymerization products of ethylene carbonate with thiophene, which protects the electrolyte components from further decomposition. The formation mechanism of the polymeric film was modeled using quantum chemistry calculations, which shows good agreement with the experimental data.

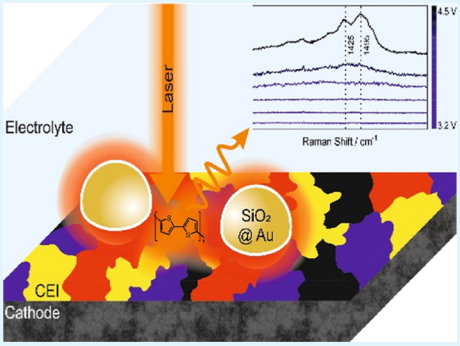


**KEYWORDS:** *lithium-ion batteries, high-voltage cathode, thiophene, interphase, operando SHINERS*

## 1. INTRODUCTION

Increasing the cell voltage is considered a primary strategy for enhancing the specific energy of lithium-ion batteries (LIBs).[1−6] However, the performance of high-voltage LIBs is hindered by structural changes and electrochemical instabilities of the state-of-the-art cathode active materials and electrolytes, respectively.[1,4,5,7] A high degree of delithiation at high potentials (above 4.3 V vs $LiLi^+$) leads to thermodynamic instabilities of the layered transition metal oxides, $LiNi_xCo_yMn_{1-x-y}O_2$ (NMC), hampering their large achievable capacities and cycle life.[1,5−7] This results in a phase change in the cathode active materials, followed by transition metal dissolution into the electrolyte, which eventually affects the interphase properties of the cathode and anode.[1,6,8] Another detrimental effect of high voltages on the cathode is elevated side reactions on the surface due to electrolyte decomposition. The result of the aggravated side reactions is the loss of active lithium and the formation of a resistive cathode electrolyte interphase (CEI), which limits Li-ion transport.[9−11]

The significant effect of high voltages on the cycling of LIB cells can be mitigated through surface-coating agents to reduce side reactions and the exposure of transition metals to the electrolyte.[1,2,12−16] Another alternative approach to minimize failure mechanisms at high voltages is incorporating film-forming additives.[17−19] However, implementing different film-forming additives is vastly recognized as a trial-and-error approach toward obtaining ideal interphase properties. To systematically design efficient CEIs for high-voltage applications, understanding the degradation and failure mechanisms to develop mitigation strategies is necessary. Furthermore, these techniques should enable robust acquisition strategies to probe the working mechanism of the film-forming additives under real working conditions. Significant efforts have been devoted to developing spectroscopic techniques to explore different properties of interphases on high-voltage cathodes. However, studies on operando investigations of the CEI are rare, and the number of utilized techniques is limited.

In 2017, Lu et al. employed atomic force microscopy to gain visual information about the CEI development on $LiCoO_2$ during charge/discharge cycling.[20] In 2015, Matsui et al. utilized operando Fourier transform infrared spectroscopy (FTIR) to investigate the interphases on $LiMn_2O_4$ and graphite electrodes in a carbonate-based electrolyte. In their

Received: October 5, 2022
Accepted: December 22, 2022
Published: January 26, 2023

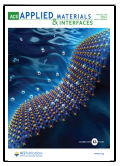

study, they were able to show solid electrolyte interphase (SEI) formation on the negative electrode, while no CEI was reported on $LiMn_2O_4$.[21] In 2019, Meng et al. investigated CEI formation on $Li_{1.2}Ni_{0.2}Mn_{0.6}O_2$ electrodes in a carbonate-based electrolyte. Using operando ATR−FTIR spectroscopy, they indirectly detected CEI formation on the positive electrode.[22]

These studies are examples of CEI investigations of different cathodes. However, a comprehensive and systematic study of the interphase composition formed directly on the cathode surface under real working conditions requires further realization through the development of complementary techniques. This is partly due to the intrinsic signal acquisition and technical challenges with these techniques to investigate the nanometric thin CEI in LIBs.

Raman spectroscopy can potentially offer trace analysis of materials suitable for interphase investigation. However, conventional Raman spectroscopy has mainly been employed in battery research to characterize the composition and nature of the electrochemical processes in the bulk electrodes, failing largely to probe interfacial chemistries.[23−28] This is mainly due to the very inefficient Raman scattering process and the micrometric skin depth of Raman, which result in very low sensitivities for detecting nanometric thin interphases.[23,24] Both insufficiencies of conventional Raman can be mitigated by near-field Raman spectroscopy.[24,26,29,30] This can be achieved by introducing plasmonic active nanoparticles to the surface of the electrodes in a technique known as shell-isolated nanoparticle-enhanced Raman spectroscopy (SHINERS). Optimized plasmonic nanoparticles on the surface of the electrode work as electromagnetic resonators to create a strong near-field in their vicinity and increase the efficiency of Raman scattering. Furthermore, these nanoparticles are covered with an inert shell to avoid interference with the cell components.

Different groups already utilized SHINERS to gain insights into the mechanisms of interphase formation on various anode materials.[23] However, to our knowledge, no operando SHINERS study has been performed on the analysis of CEI on NMC electrodes.

In this paper, we introduced operando SHINERS as a reliable technique to monitor the CEI properties in the presence of thiophene film-forming additives for high-voltage applications. In previous studies, thiophene and thiophene derivatives have been implemented as CEI additives for several cathode materials.[31−35] In this work, however, we first performed a detailed electrochemical investigation of thiophene as an effective film-forming additive on NMC111||graphite cell chemistry for high-voltage applications. The cell performance was significantly improved at the optimized concentration of thiophene by avoiding electrolyte decomposition, and processes leading to cathode failure at high voltages of 4.5 V. The formation of a stable and efficient CEI was realized through the presence of polythiophene and ethylene carbonate (EC) copolymerization with thiophene monomers captured by operando SHINERS. Operando SHINERS provides mechanistic insights into the formation of the polymeric film on NMC111 cathodes and the origin of the high performance observed in the high-voltage LIBs in the presence of thiophene. The experimental findings are complemented by quantum chemistry (QC) calculations at the highly accurate G4MP2 level of theory.[36]

## 2. EXPERIMENTAL SECTION

**2.1. Electrode Preparation.** Electrode sheets were purchased from Custom Cells Itzehoe GmbH. NMC111 and graphite electrodes with a 14 and 15 mm diameter were punched out and dried for 12 h at 120 °C under a reduced atmosphere. The NMC111 electrodes consisted of 90 wt % active material with a specific capacity of 145 mA h $g^{-1}$, resulting in a mass loading of 1.0 mA h $cm^{-2}$. The graphite electrodes consisted of 95 wt % active material with a specific capacity of 350 mA h $g^{-1}$, resulting in a mass loading of 1.2 mA h $cm^{-2}$. For potentiostatic measurements, NMC111 and graphite electrodes with a 12 mm diameter were prepared similarly. The prepared electrodes were stored in an argon-filled glovebox (MBraun, $H_2O$ content below 1 ppm and $O_2$ content below 1 ppm) or a dry room (dew point: −50 °C).

**2.2. Electrolyte Preparation.** The baseline electrolyte consisting of 1 M $LiPF_6$ in EC/DEC, 1:1 by weight (E-Lyte Innovations, battery grade), was first prepared. For preparing the thiophene-containing electrolytes (thiophene was purchased from Sigma-Aldrich, >99%), a stock solution of EC/DEC, 1:1 by weight, was prepared. Next, adequate amounts of thiophene and $LiPF_6$ salt were added to a volumetric flask and filled with the EC/DEC 1:1 solution to reach the defined volume. The following thiophene concentrations were prepared: 0.012, 0.043, 0.072, 0.096, and 0.12 M. All electrolytes were made in an argon-filled glovebox and stored in a dry room (dew point: −50 °C).

**2.3. Cell Assembly.** For galvanostatic investigations of the electrolytes, 2032-type NMC111||graphite coin-cells (two-electrode setup) were assembled. One layer of Celgard 2500 (polypropylene, 16 mm diameter) was used as the separator. The cells were filled with 60 μL of electrolytes. Cell assembly was performed in a dry room. For each investigated system, three cells were built to ensure reproducibility.

For potentiostatic investigation, Swagelok-type T-cells were used, with NMC111 electrodes as the working electrode (WE), graphite as the counter electrode (CE), and Li−metal as the reference electrode (RE). One layer of Whatman separator (glass fiber) with a 13 and 10 mm diameter was used to separate the electrodes and soaked with 120 and 80 μL of electrolyte. To ensure electronic isolation, the interior of the cells was covered with Mylar foil. All of the Swagelok cells were prepared in an argon-filled glovebox. Swagelok-type T-cells were chosen for potentiostatic investigation in this work because they enabled us to use a three-electrode cell configuration, allowing precise control of the cathode potential versus the reference electrode for investigating the process at the CEI.

**2.4. Electrochemical Investigation.** The additive's influence on the cells' electrochemical performance was studied by constant current charge/discharge cycling of the prepared NMC111||graphite full-cells at the potential range of 2.8−4.5 V and a *C*-rate of 1 C. Before cycling, the cells rested for 24 h and then cycled for three constant current voltage cycles at a *C*-rate of 0.1 and 0.333 C each. Cycling was performed using a Maccor 4000 battery testing system in a temperature-controlled chamber at 20 °C. Cyclic voltammetry (CV) experiments were performed using an Autolab potentiostat/galvanostat (Metrohm) controlled using NOVA 2.1 software. Before the CV measurement, the cells rested for 10 h to ensure sufficient wetting and reaching constant open-circuit potential (OCP). The CVs were performed in a voltage range of 2.8 to 4.5 V versus Li|$Li^+$ at a scan rate of 150 μV $s^{-1}$. For each cell, three CV cycles were performed.

**2.5. Electrochemical Impedance Spectroscopy.** Electrochemical impedance spectroscopy (EIS) measurements were performed to investigate the changes in the impedance of the cell components due to thiophene-induced interphase formation. EIS measurements were carried out using an Autolab potentiostat/galvanostat (Metrohm) equipped with an impedance module and controlled using NOVA 2.1 software. For the measurements, NMC111||graphite Li-FUN commercial pouch cells were prepared and cycled in a voltage range between 2.8 and 4.5 V at a *C*-rate of 1 C. Before preparation, the pouch cells were dried overnight at 90 °C in a



https://doi.org/10.1021/acsami.2c17958
ACS Appl. Mater. Interfaces 2023, 15, 6676−6686

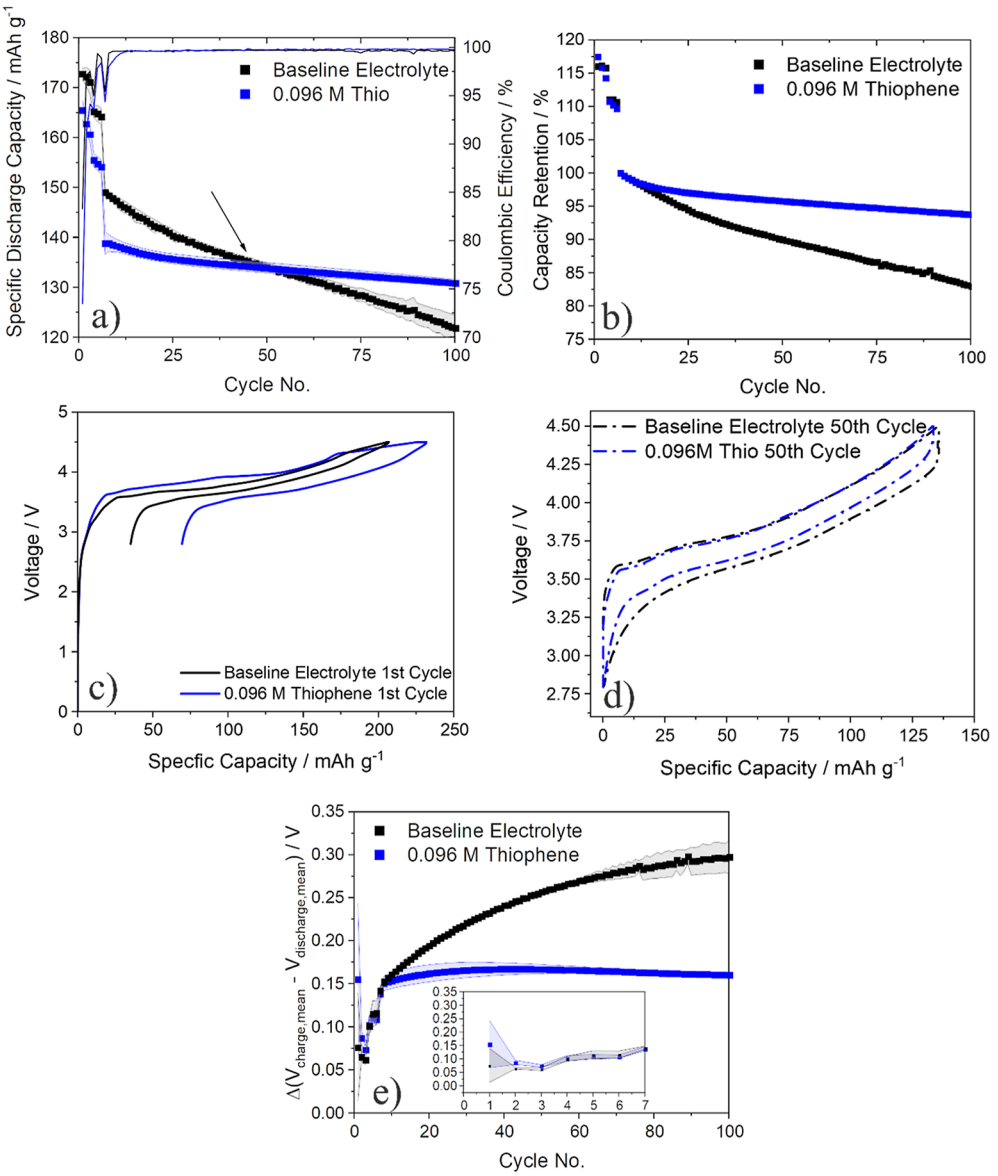


**Figure 1.** (a) Specific delithiation capacity, corresponding coulombic efficiencies, and (b) capacity retention of NMC111||graphite full-cells (two electrode configuration) with electrolytes, featuring the optimized concentration of thiophene. Capacity retention was calculated based on the seventh cycle (the first cycle after formation). Voltage−capacity histograms of the (c) first and (d) 50th cycle observed in NMC111||graphite full-cells with the baseline electrolyte and baseline electrolyte + 0.096 M thiophene. (e) Plotted difference of the mean charge voltage and the mean discharge voltage for an NMC111||graphite full-cell as an estimation for cell impedance for the baseline electrolyte (black) and baseline electrolyte + 0.096 M thiophene (blue).

reduced atmosphere. The assembly of the cells was conducted in a dry room. 700 $\mu$L of electrolyte was used to fill the cells. EIS measurements were performed at a voltage of 3.5 V for every charge and discharge cycle in a frequency range of 100,000 to 0.01 Hz.

**2.6. Nanoparticle Synthesis.** For the SHINERS measurements, 55 nm $SiO_2$-coated Au-NPs were synthesized according to the procedure suggested by Li et al.[37] Briefly, 100 mL of 0.01 wt % $AuCl_3$ (99.995%, Sigma-Aldrich) solution was added into a round-bottom flask. The solution was boiled, and 0.7 mL of a 1 wt % sodium citrate solution (Reference Standard, USP) was added to the boiling solution while stirring. The mixture was stirred for 30 min under reflux to obtain Au-NPs with a size of 55 nm. For coating, 30 mL of the 55 nm Au-NP solution was added into a round-bottom flask. Under vigorous stirring, 0.4 mL of a 1.0 mM 3-aminopropyltrimethoxysilane solution (APTMS, 97%, Sigma-Aldrich) was added. The mixture was stirred for 15 min at room temperature. Afterward, 2.4 mL of a 0.54 wt % sodium trisilicate solution (reagent grade, Sigma-Aldrich) (pH = 10; adjusted with HCl) was added. The mixture was heated to 90 °C and stirred for 60 min. Subsequently, the mixture was cooled in an ice bath. To wash the coated NPs, the mixture was centrifuged at 4500 rpm for 10 min. The supernatant was removed and replaced with water. The washing step was repeated twice.[37] All used glassware was cleaned with aqua regia beforehand. Milli-Q-water (Merck, 18.2 MΩ·$cm^{-1}$) was used in all the steps.

To ensure a complete coating, a 10 mM pyridine solution was added to the NPs. In the case of an incomplete coating, pyridine coordinates with gold atoms accessed in the pinholes of the NPs, showing characteristic peaks at 1012 and 1037 $cm^{-1}$ (see Figure S1a). However, these peaks were absent in the coated NPs used in this study. The size of the synthesized NPs was checked by the scanning electron microscopy (SEM) technique (see Figure S1b).

**2.7. Raman Sample Preparation.** For applying the coated NPs to the surface of the investigated electrode, it was necessary to transfer the NPs to isopropanol before casting them to the surface of the


https://doi.org/10.1021/acsami.2c17958
ACS Appl. Mater. Interfaces 2023, 15, 6676−6686

electrodes. Therefore, the aqueous solution of NP was centrifuged for 10 min at 4500 rpm, and the supernatant was decanted and replaced with isopropanol. The emerging solution was centrifuged again. This time, two-thirds of the supernatant was removed, and 60 $\mu$L of the concentrated NP suspension was drop-cast to the surface of the electrode. After solvent evaporation, another 40 $\mu$L of the NP suspension was added to the surface. The electrodes were dried at 60 °C for at least 2 h in the reduced atmosphere to remove the solvent and water residues. An airtight optical cell (EL-CELL ECC-Opto-Std) with a glass window was used for the Raman measurement. For the operando SHINERS investigation, an NMC111||graphite two-electrode full-cell setup was chosen. Both electrodes have their active material facing the glass window and are separated by one layer of Celgard 2500. An aluminum mesh was placed above the working electrode to ensure sufficient wetting and ionic diffusion on the sides of the electrodes. Finally, approximately 200 $\mu$L of electrolyte was added to the optical cell. Additionally, NMC111||Li−metal cells were prepared similarly. A schematic of the cell setup is displayed in Figure S2. All cells were prepared in an argon-filled glovebox.

Galvanostatic cycling and CVs were performed during the operando SHINERS measurements using an Autolab potentiostat/galvanostat PGSTAT204 (Compact-series, Metrohm) controlled with NOVA 2.1. Cycling experiments were performed at a rate of C/3 in the voltage range of 2.8 to 4.5 V, with the current calculated on the cathode's capacity. CVs were performed in a voltage range of 2.8 to 4.5 V versus Li|Li$^+$ with a scan rate of 150 $\mu$V s$^{-1}$. Before the operando measurements, all the Raman cells were rested for 1 h to ensure sufficient wetting of all the components. Note that cycling and CVs were performed at a low C-rate/scan rate to limit polarization effects, which could be potentially caused by the arrangement of the electrodes in the optical cell.

**2.8. Raman Investigation.** A Horiba Scientific confocal Raman microscope (LabRAM HR evolution, air-cooled CCD detector) was used for the Raman measurements. The sample was excited with a red laser with a wavelength of 633 nm and 10.5 mW output power at the sample, adjusted by a 10% filter to 1.05 mW with a 600 line/mm grating. The beam was focused using a 50× long-working distance objective (Carl Zeiss Microscopy, 9.2 mm, numerical aperture 0.5). Raman spectra were collected over two integrations of 50 s each. Handling the Raman microscope, collecting the spectra, and evaluating the data were done using LabSpec6.6.2 (Horiba Scientific). Before the measurement, the system was calibrated on the silicon peak at a Raman shift of 520.7 cm$^{-1}$. Raman investigations were performed during the initial charging cycle of the cell. A constant voltage step was implemented into the cycling procedure to avoid voltage drops during the measurements.

**2.9. SEM and EDX Investigations.** Scanning electron microscopy (SEM) and energy-dispersive X-ray analysis (EDX) were performed to investigate the surface of electrochemically aged NMC111 electrodes. SEM measurements were carried out using an Auriga electron microscope (Carl Zeiss microscopy) with an accelerating voltage of 3 kV. EDX investigations were performed at an accelerating voltage of 10 kV using an energy-dispersive X-ray detector (Oxford Instruments). The cycling of the NMC111 electrodes was conducted in the airtight optical Raman cell. The electrodes underwent three CV cycles in the voltage range of 2.8−4.5 V with a scan rate of 150 $\mu$V s$^{-1}$. After cycling, the electrodes were transferred into an argon-filled glovebox and washed with 100 $\mu$L EMC to remove electrolyte residues. The electrodes were dried under a reduced atmosphere for 10 min and transferred into the microscope chamber via an airtight vessel.

**2.10. Theoretical Modeling.** To elucidate the energetics of the thiophene polymerization mechanism, QC calculations were performed at the accurate but computationally expensive G4MP2 level of theory (typical error of 1 kcal/mol or 0.04 V) using the Gaussian 16 package.[36,38] The molecular structures of educts, products, and intermediates have been created by Avogadro.[39] Subsequently, the lowest-energy conformers have been obtained at the semi-empirical xtb level of theory using CREST.[40−43] Additional conformers for comparison have been generated by hand or via Open Babel.[44]

Electrochemical oxidation potentials have been computed via the Nernst equation

$$E_{ox} = \frac{\Delta G_{ox}}{nF}$$

for the respective putative oxidation reactions, characterized by their free energy difference $\Delta G_{ox}$, where $n$ is the number of electrons transferred per elementary step and $F$ is Faraday's constant (note that for reduction reactions, the sign of the above equation changes). To relate the values to the experimentally relevant Li|Li$^+$ scale, a constant shift of −1.4 V was applied.[45,46]

In all calculations, an implicit solvation model was employed to mimic the intermolecular environment in the electrolyte. The SMD and GBSA solvation models were applied for the G4MP2 and xtb calculations, respectively, both with built-in parameters for acetone showing a similar dielectric constant as liquid carbonate electrolytes.[42,46−49]

## 3. RESULTS AND DISCUSSION

**3.1. Electrochemical Results.** To investigate the role of thiophene as a film-forming additive for high-voltage applications (4.5 V), cycling measurements of NMC111|| graphite full-cells were performed at different concentrations. Figure 1 shows the discharge capacities and the corresponding coulombic efficiency, capacity retention, voltage−capacity histograms, and mean charge−discharge voltages for the benchmark and the cells at the optimized concentration of 0.096 M thiophene (see Supporting Information for all investigated concentrations).

As observed in Figure 1a, the discharge capacity of the benchmark cells exhibits an increased capacity decline with increasing cycle number, indicating fading effects known for high cut-off voltages. The capacity of the benchmark cells constantly declined and, after 100 cycles, reached 82% of the original capacity. In contrast, for the cells cycled with the optimum concentrations of thiophene, the fading significantly reduced, despite lower coulombic efficiencies in the initial charge/discharge cycles. These observations are also reflected in the capacity retention values, shown in Figure 1b. It is clearly seen that the capacity retention of the cells cycled with the baseline electrolyte decreased significantly faster than that of those cycled with the thiophene-containing electrolyte. After 100 cycles, the capacity of the benchmark cell was at 82% of its original value, while the thiophene-containing cells showed a capacity retention of 94%.

The corresponding voltage−capacity histograms of the first cycle (0.1 C) in the baseline electrolyte and 0.096 M thiophene in Figure 1c,d also exhibit major differences. For the cells with the thiophene-containing electrolyte, a plateau was observed at ∼4.3 V in the first cycle, while no similar plateau was observed for the baseline electrolyte. The corresponding d$Q$/d$V$ curves of the charge/discharge cycles, displayed in Figure S5a,b, indicate that the plateau in 4.3 V diminishes mainly after the first cycle. These histograms also outline the formation of a more effective CEI, which affects the battery performance at higher cycle numbers. In Figure 1d, the capacity−voltage histogram of the cell with thiophene-containing electrolyte shows a reduced voltage hysteresis compared to the benchmark cell in the 50th cycle. Furthermore, the increased initial voltage hysteresis observed in the cell with thiophene accounts for the lower initial Coulombic efficiencies (CE) in Figure 1a. The observed


https://doi.org/10.1021/acsami.2c17958
ACS Appl. Mater. Interfaces 2023, 15, 6676−6686

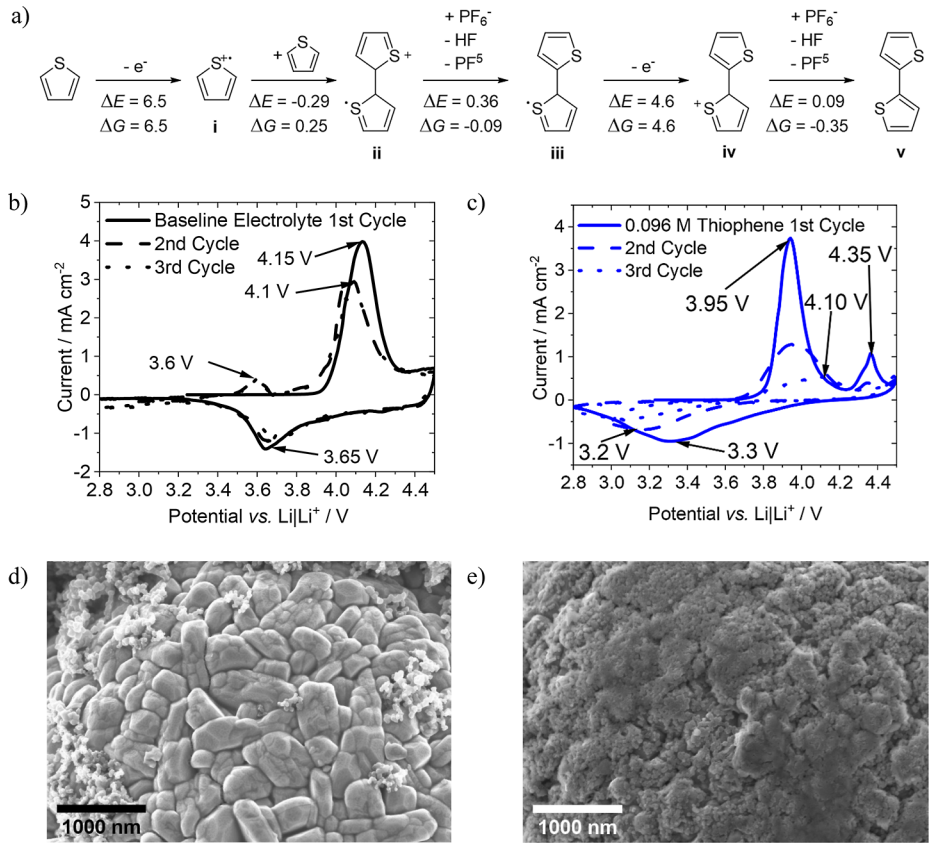


**Figure 2.** (a) Putative reaction mechanism of thiophene oxidation and electropolymerization with energy differences $\Delta E$ (computed at 0 K) and free energy differences $\Delta G$ (computed at 298 K). Units are electron volts. The first three cycles of the cyclic voltammograms of (b) the baseline electrolyte and (c) the baseline electrolyte + 0.096 M thiophene, recorded in NMC111||graphite full-cells (three-electrode configuration) with a scan rate of 150 $\mu$V/s. Relevant redox peaks are marked with arrows. (d + e) SEM images of the surface of NMC111 electrodes at a magnification of 25,000. (d) is taken from a pristine electrode, while (e) is taken from an electrode cycled in the baseline electrolyte + 0.096 M thiophene.

plateau, in combination with the lower CE for the cells containing thiophene, indicates charge-consuming reactions in the first cycle due to the presence of the additive.

Figure 1e shows the difference between the mean charge and discharge voltages ($\Delta V$) plotted against the cycle number as an estimation for the internal resistance.[50,51] Despite a distinct difference in the first cycle ($\Delta V_{baseline}$ = 0.06 V vs $\Delta V_{thiophene}$ = 0.15 V), the $\Delta V$ of the thiophene-containing cells only showed slightly higher values within the first seven cycles. At higher cycle numbers, however, it was observed that the $\Delta V$ for the cells with the baseline electrolyte increased significantly to ~0.3 V after 100 cycles, while the $\Delta V$ for the thiophene-containing cells leveled out at ~0.15 V after 100 cycles. The higher $\Delta V$ for the thiophene-containing cells observed for the first cycle can be assigned to the decomposition of the additive, matching with the plateau in the voltage−capacity histograms, displayed in Figure 1c. (Note that the sudden increase in the $\Delta V$ of both electrolytes after the sixth cycle is due to the increased C-rate (cycling at 1 C), as the seventh cycle is the first cycle after the formation cycles (three cycles at 0.1 and 0.333 C.)) However, the fact that the $\Delta V$ for the thiophene-containing cells remained almost constant while an ongoing increase of the $\Delta V$ for the baseline electrolyte was observed, indicates that the presence of thiophene leads to the formation of a more effective interphase.[52,53] The increased $\Delta V$ for the thiophene-containing cells during the initial cycles also explains the decreased capacity of these cells observed during cycling (Figure 1a). Increased resistance results in higher over-potentials, leading to an artificial increase in the cell voltage and, therefore, an earlier hitting of the cut-off potential at 4.5 V.[52]

Besides $\Delta V$ analysis, in situ EIS was performed to investigate changes in the cell's impedance in the first 20 cycles. It was found that the thiophene-containing cell exhibited a higher interphase resistance compared to the cell with the baseline electrolyte in the initial cycles. However, the resistance for the benchmark cell increased with a higher cycle number, while the resistance for the thiophene-containing cell remained almost constant. These results agree with the $\Delta V$ analysis in Figure 1e (more information about the EIS results can be found in the Supporting Information).

QC calculations on the oxidation of thiophene were performed to explore the observed phenomena more precisely. For oxidation of a single thiophene molecule, we found a value of 5.1 V versus Li|Li$^+$, which is lower than the respective potentials for single carbonate molecules (5.7 V vs Li|Li$^+$) and thus consistent with thiophene oxidation prior to degradation of the carbonate compounds.[17,54] An even higher value of 7.4 V versus Li|Li$^+$ was found from the HOMO of thiophene at the CCSD(T)/6-31G(d) step in G4MP2, underscoring the effect of molecular relaxation upon electron transfer. On the other hand, when placing a $PF_6^-$ anion near the thiophene molecule in the calculations, the oxidation potential was lowered to 4.7 V versus Li|Li$^+$. However, calculations on isolated molecules or clusters only provided limited insights into the actual mechanism because redox potentials are thermodynamic


https://doi.org/10.1021/acsami.2c17958
ACS Appl. Mater. Interfaces 2023, 15, 6676−6686

quantities and therefore required the knowledge of viable reaction mechanisms of the electrochemical electrolyte decomposition.[45,46,54−56] Consequently, we additionally computed the free-energy profile of the presumed electropolymerization mechanism of thiophene, as shown in Figure 2a.

After an initial oxidation step, a thiophene molecule may encounter another one to form a dimer. The excess positive charge may then be stabilized by proton transfer from the $\alpha$ carbon atom, which then becomes $sp^2$ hybridized again. In fact, such proton transfer events are supported by other recent QC calculations.[45,46,54,57] As an example, we assume transfer to a $PF_6^-$ anion in the following—leading to the formation of HF and $PF_5$—although the carbonate molecules, the NMC interface, or trace water could likewise serve as proton acceptors. (Note that the energy differences for different proton transfer mechanisms are usually small.)[17,45,46,54] It should be noted that the formation of HF and $PF_5$ could be a plausible explanation for the decreased discharge capacity of the thiophene-containing cells within the initial cycles in Figure 1a.

Initially, a thiophene molecule is oxidized (i) with a free energy difference of $\Delta G$ = 6.5 eV (i.e., on the absolute potential scale, corresponding to 5.1 V on the Li|Li$^+$ scale (see above); note that as only one electron is transferred per elementary reaction, energies in electron volts (eVs) are equivalent to potentials in volts). Subsequently, the thiophene radical can form a dimer (ii) when encountering another thiophene molecule with a free energy difference of 0.25 eV, which can be further stabilized by deprotonation (iii) with a free energy gain of −0.09 eV (see above for detailed proton transfer reaction). The second oxidation step of the thus obtained neutral thiophene dimer radical (iv) is associated with a smaller ionization free energy of $\Delta G$ = 4.6 eV (3.2 eV on the Li|Li$^+$ scale) and is, therefore, likely to occur after the first oxidation step. Moreover, the resulting closed-shell thiophene dimer cation (v) can be further stabilized by another deprotonation step with a significant energy gain of $\Delta G$ = −0.35 eV. The total free energy difference of the dimerization, including two oxidation and two deprotonation steps, amounts to $\Delta G$ = 10.9 eV (5.5 eV per transferred electron), equivalent to an oxidation potential of 4.1 V versus Li|Li$^+$. Given the assumptions in the calculations, this is in good agreement with the experimental data, as proved further by CV. The slight differences between the calculated potential for the formation of polythiophene and the experimental results are due to the simplified system used for the QC calculations.

The CVs in the potential range of 2.8−4.5 V versus Li|Li$^+$ are displayed in Figure 2b,c. In the first cycle, the CV of the baseline electrolyte in Figure 2b is characterized by a single main peak in each sweep direction located at +4.15 and +3.65 V versus Li|Li$^+$. These peaks were assigned to Li-ion extraction from the cathode and Li-ion insertion in the reverse anodic process.[58] The Li-ion insertion and extraction peaks were also present in the CV of the thiophene-containing cell in Figure 2c located at 3.3 and 3.95 V versus Li|Li$^+$. For the second and third cycles, however, shifts in these peaks were observed. In the CV of the baseline electrolyte, a shift of the delithiation peak to 4.1 V was recorded, while for the thiophene-containing electrolyte, a shift to higher values was observed. Moreover, the CV of the thiophene-containing cell showed a shift of the Li-ion insertion peak in the second cycle to 3.2 V, while no similar shifting was recorded for the cell with the baseline electrolyte. In addition, a decreased current density was observed for both CVs in the second and third cycles. While for the cell with the baseline electrolyte, only a moderate decrease in the current density was recorded, the cell-containing thiophene showed a severe decline in the current density. Furthermore, additional peaks were observed within the CVs of the baseline and thiophene-containing cells. In the CV of the benchmark cell, an additional peak at 3.6 V versus Li|Li$^+$ was detected for the second and third cycles. As this peak did not appear in the first cycle, we suggest that it can be attributed to subsequent reactions of electrolyte decomposition products on the NMC111 electrode, which were initially formed on the graphite electrode and dissolved in the electrolyte. In the first cycle, an additional peak at 4.35 V versus Li|Li$^+$ in the cell with the thiophene-containing electrolyte was observed.

As proved via the QC calculations of the reaction mechanism discussed above, the peak at 4.35 V versus Li|Li$^+$ can be attributed to the oxidation of thiophene and the formation of radical cation species, leading to the formation of polythiophene. Also, a direct correlation of the CV in Figure 2c with the d$Q$/d$V$ in Figure S5 showed that the presence of the thiophene additive accounts for the oxidation peak located around 4.35 V in both measurements. As no additional peaks were observed for the second and third cycles of the CV at potentials higher than 4.35 V versus Li|Li$^+$, it can be assumed that the formed interphase is stable against further oxidation and, therefore, is capable of protecting the electrolyte from ongoing oxidation on the surface of the cathode. In addition, the CV data of the thiophene-containing cell indicate that most of the polymerization of the additive occurs during the first cycle, as the intensity of the corresponding peak decreases significantly from the first to the second cycle. For the third cycle, no peak at 4.35 V versus Li|Li$^+$ was observed, indicating that the polymerization process had already been completed.

The suggested formation of polythiophene accounts for other effects observed in the CV of the thiophene-containing cell. As discussed in an earlier section (Figure 1e), the formation of polythiophene leads to increased cell resistance, resulting in higher overpotentials and, therefore, limitations in charge transfer at the surface of the electrodes. This causes a decrease in the current density relating to limited charge extraction/insertion from/into the cathode.

Another notable difference in these CVs was the increased value for the peak-to-peak separation in the cell with thiophene. The peak-to-peak separation of the cell with the baseline electrolyte was around 450 mV, while in the case of 0.096 M thiophene, this value was about 750 mV for the second cycle. This suggested a Li-ion diffusion-dominated process for the insertion/extraction of the NMC cathode.[59,60] In other words, the diffusion length of Li-ions from the electrolyte into/out of the cathode is longer in the cell containing thiophene, indicating that Li ions have to pass through an intermediate phase during the insertion/extraction processes formed in the presence of the thiophene additive.

**3.2. Surface Investigation via SEM and EDX.** To gain visual confirmation on the formation of the thiophene-based interphase on the surface of NMC111, SEM investigations of electrodes, cycled in the baseline and 0.096 M thiophene-containing electrolytes, were performed. Figure 2d,e displays SEM images of the pristine NMC111 electrode and the electrode cycled in the thiophene-containing electrolyte. While the crystals of the cathode active material and small patches of


https://doi.org/10.1021/acsami.2c17958
ACS Appl. Mater. Interfaces 2023, 15, 6676−6686

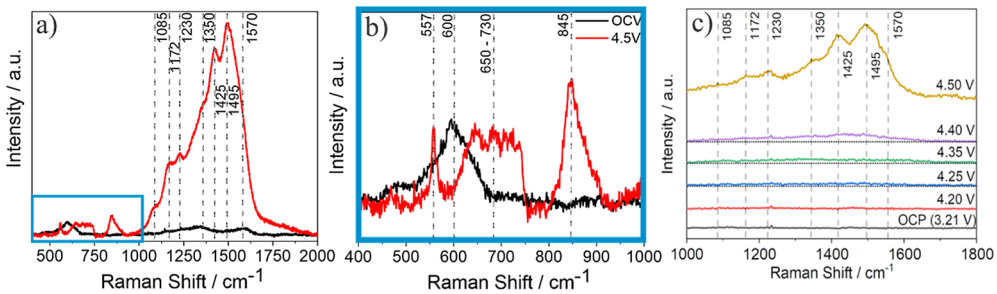


**Figure 3.** Raman spectrum of the interphase formed on an NMC111 electrode cycled with the baseline electrolyte + 0.096 M thiophene (two electrode setup, NMC111||graphite). (a) Full-range spectrum from 400 to 2000 $cm^{-1}$ and (b) magnification of the spectral range from 400 to 1000 $cm^{-1}$. The spectra are recorded at the OCV (black) with the cell voltage of 4.5 V (red). Relevant peaks are marked with dashed lines. (c) Raman spectra of the interphase formed on the NMC111 electrode, cycled with the baseline electrolyte + 0.096 M thiophene (two electrode setup, NMC111||Li−metal) at different potentials vs Li|$Li^+$. Dotted lines are added to the background of the spectra recorded at 4.25, 4.35, and 4.40 V to highlight changes in the background intensity. Relevant peaks are marked with dashed lines. All the potentials are referenced against the Li|$Li^+$ electrode.

the binder can be seen clearly for the pristine electrode (Figure 2d), a cauliflower-like layer covering the surface of the active material can be observed for the electrode cycled with the thiophene-containing electrolyte (Figure 2e). Furthermore, the formation of a surface layer on the active material of the cathode cycled in the baseline electrolyte can be observed. However, the layer only covers patches of the active material and does not provide complete coverage of the NMC particles (see Figure S7).

To link the observed interphase to the formation of thiophene-based products on the surface of NMC111 electrodes, EDX measurements were performed. This investigation showed the presence of sulfur on the active material particle in Figure S7, suggesting the formation of the thiophene-based interphase on the surface of the active material. This finding agrees with our suggested oxidative polymerization mechanism on the active materials of the NMC cathode. The corresponding figures for EDX investigation and SEM images of the electrodes can be found in Figure S7 in the Supporting Information.

**3.3. Operando SHINERS Investigation.** To gain a fundamental understanding of the nature and dynamics of the CEI formation on the NMC cathode, an operando analysis using an interfacial sensitive technique is required to clarify the origin of the improvement in the LIB performance. As shown in Figure 3, operando SHINERS measurements were performed on the cathode in the presence of 0.096 M thiophene in an NMC111||graphite and NMC111||Li−metal cell.

As shown in Figure 3, the open-circuit voltage (OCV) spectrum was indicated, with three peaks assigned to the electrode components of the cathode. The peak around 600 $cm^{-1}$ was assigned to the lattice vibration of the active material in the NMC111 electrode, which was only observed at the OCV.[61] This peak disappeared at higher voltages due to the lattice phase transition and increased electronic conductivity of the delithiated cathode, resulting in a lower skin depth of the Raman scattering process.[62] The peaks around 1350 and 1570 $cm^{-1}$ correlate to the D and G bands of the carbonaceous material present as the conductive agent in the cathode.[63−65] Besides these peaks, at 4.5 V, several new peaks appeared due to CEI formation. The peak around 557 $cm^{-1}$ cannot be clearly assigned; however, we suggest it correlates with phase transitions occurring at high voltages within the cathode active material. The peaks located in the region between 650 and 730 $cm^{-1}$ can be attributed to C−C and C−S−C ring deformation vibrations.[66−69] The peak around 845 $cm^{-1}$ can be assigned to C−H deformation vibrations,[66] while the peak around 1085 $cm^{-1}$ correlates to C−C stretching and C−H wedging.[67−69] The peaks around 1172 and 1230 $cm^{-1}$ can be attributed to the anti and regular C−C stretching vibrations, respectively.[67,68] The two prominent peaks around 1425 and 1495 $cm^{-1}$ can be assigned to $C_\alpha$=$C_\beta$ ring stretching. The latter is assigned to the anti-ring stretching band.[66−68]

Comparing the operando SHINERS spectra of the cell containing thiophene with the benchmark (Figure S8), the two prominent peaks around 1425 and 1495 $cm^{-1}$, in correlation to the peaks in the region between 650 and 730 $cm^{-1}$, can be assigned to the formation of polythiophene on the NMC111 surface at high voltages. As these peaks only appeared at high voltages and in agreement with the electrochemical measurements and theoretical calculations, it can be concluded that polythiophene is the dominant product of the formed CEI.

In addition, it was possible to determine the exact potential of the thiophene electropolymerization on the NMC surface by performing operando SHINERS in an NMC111||Li−metal cell (Figure 3c). This is manifested by the increased intensity of the background in the Raman spectra between 1300 and 1600 $cm^{-1}$ at higher potentials. The discussed increase began at a potential of 4.35 V versus Li|$Li^+$; however, significant changes in the background intensity were observable at 4.4 V for the first time, indicating that the formation of polythiophene only occurred on a small scale at the potentials below 4.4 V versus Li|$Li^+$. These results are in good agreement with the electrochemical experiments. Note that Li−metal was chosen as a counter and reference electrode for this investigation to precisely determine the potential of the polymerization reaction and to correlate the obtained results with the electrochemical experiments. The full ranges of the spectra are shown in Figure S9.

Interestingly, besides the prominent formation of polythiophene shown in Figure 3b,c, operando SHINERS caught the presence of co-products in the interphase. The active vibration band around 1172 $cm^{-1}$, attributed to C−C stretching vibrations, can be assigned to the decomposition products of solvents at high voltages on the NMC111 surface. We performed QC calculations to check the possibility of the copolymerization of EC and thiophene, facilitated by an EC radical attacking a thiophene molecule. The suggested mechanism is similar to the already discussed polymerization


https://doi.org/10.1021/acsami.2c17958
ACS Appl. Mater. Interfaces 2023, 15, 6676−6686

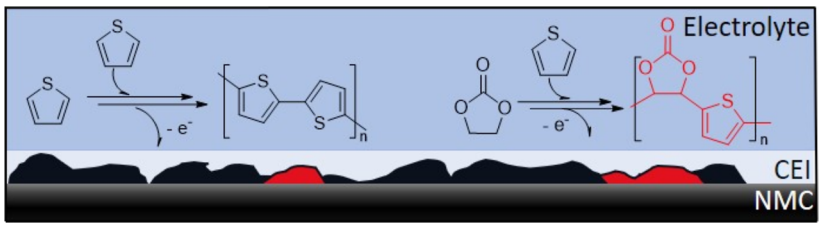


**Figure 4.** Schematic representation of the polymer-based interphase on the NMC111 surface and the suggested polymerization reactions and their products; polythiophene (black) and the EC−thiophene copolymer (red).

of thiophene. In the first step, EC is oxidized, resulting in the formation of an EC radical cation. The radical cation can then be deprotonated by a $PF_6$ anion, giving HF and $PF_5$. For this step, an oxidation potential of 5.7 V versus Li|Li$^+$ was calculated, in agreement with literature values in the range of 5.2−6.0 V.[45,46] For the subsequent addition of thiophene to the EC radical, a low energy barrier of 0.4−0.5 eV was calculated, followed by a stabilizing energy gain of 0.7−0.6 eV for the overall reaction, making the suggested mechanism thermodynamically favorable. From this point on, the formed EC−thiophene dimer can further react with other EC or thiophene molecules, forming the observed copolymer (Figure 4).

Besides the copolymerization, we also investigated the possibility of EC polymerization, leading to the formation of a polycarbonate. For this reaction, two mechanisms (radical and anionic) were calculated. Similar to the copolymerization mechanism, the oxidation and subsequent deprotonation of EC by a $PF_6$ anion were suggested as the first step for the radical mechanism. However, for the addition of another EC molecule to the EC radical, a high energy barrier of 1.5−1.6 eV was found. Also, the subsequent formation of polycarbonate only comes with a small energy gain of 0.1 eV. In contrast to the radical mechanism, the anionic formation of polycarbonate is more plausible. As the first step of the anionic mechanism, we suggested a nucleophilic attack of $F^-$ on an EC molecule. A moderate energy barrier of 0.7−0.8 eV was calculated for this attack. The fluorination leads to a ring-opening of the attacked EC molecule, leaving it as a linear carbonate with a negative charge on the carbonate group. A slight gain in energy of 0.1 eV was calculated for the overall reaction. This negatively charged carbonate can further attack other EC molecules in the following reactions, starting the cascade of anionic polymerization reactions. As the initiating fluoride anion is a side product of the polymerization of thiophene (see Figure 2a), it can be stated that both reactions occur at the same potential of 4.35 V versus Li|Li$^+$. Detailed schematics of the discussed mechanisms and structures of the resulting polymers are shown in Figure S10.

Nevertheless, it has to be noted that the electropolymerization of thiophene is clearly favored over the suggested copolymerization mechanisms based on the calculated energetics. However, due to the abundance of EC in the electrolyte, the copolymerization of EC and thiophene on a small scale is plausible, manifesting in the observed peaks around 1172 cm$^{-1}$ in the Raman spectra.

Concluding from the calculations of different polymerization mechanisms and Raman investigations, we state that the interphase formed on the surface of the NMC cathode mostly consists of polythiophene. However, a minor interphase component is possibly an EC−thiophene copolymer (see Figure 4b).

## 4. CONCLUSIONS

In the present study, we introduced operando SHINERS as a surface-sensitive technique to capture the presence of the CEI components and elucidate the underlying mechanisms involved with interphase formation. We investigated the role of thiophene as a high-voltage film-forming additive on NMC111 electrodes and evinced the beneficial effect of thiophene due to the formation of an effective CEI. A correlative analysis of the electrochemical data with operando SHINERS and theoretical calculations proved anodic oxidation of thiophene, resulting in the formation of a polythiophene-based interphase on the cathode's surface at high voltages.

SEM and EDX investigations additionally confirmed polythiophene as the main component of the interphase. However, the presence of other components was detected by operando SHINERS. According to the theoretical calculations, this side product is most likely to be an EC−thiophene copolymer. Based on the results of this work, we state that operando SHINERS is a powerful technique to investigate the interphases in energy storage systems under real working conditions.

## ■ ASSOCIATED CONTENT

### Supporting Information

The Supporting Information is available free of charge at https://pubs.acs.org/doi/10.1021/acsami.2c17958.

Characterization of the synthesized nanoparticles; schematic setup of the utilized optical cell; results of the electrochemical performance of all investigated thiophene concentrations; additional voltage−capacity histograms, dQ/dVs, CVs, and SEM pictures; additional and full-range Raman spectra; and reaction mechanisms of copolymerization of EC and thiophene (PDF)

## ■ AUTHOR INFORMATION

### Corresponding Author

**Masoud Baghernejad** − *Helmholtz-Institute Münster, IEK-12, Forschungszentrum Jülich GmbH, 48149 Münster, Germany;* orcid.org/0000-0002-2754-6623; Email: b.masoud@fz-juelich.de

### Authors

**Felix Pfeiffer** − *Helmholtz-Institute Münster, IEK-12, Forschungszentrum Jülich GmbH, 48149 Münster, Germany;* orcid.org/0000-0002-3897-2062

**Diddo Diddens** − *Helmholtz-Institute Münster, IEK-12, Forschungszentrum Jülich GmbH, 48149 Münster, Germany;* orcid.org/0000-0002-2137-1332

**Matthias Weiling** − *Helmholtz-Institute Münster, IEK-12, Forschungszentrum Jülich GmbH, 48149 Münster, Germany;* orcid.org/0000-0002-0987-4404



https://doi.org/10.1021/acsami.2c17958
ACS Appl. Mater. Interfaces 2023, 15, 6676−6686

Complete contact information is available at:
https://pubs.acs.org/10.1021/acsami.2c17958

### Notes

The authors declare no competing financial interest.

## ■ ACKNOWLEDGMENTS

Financial support from the German Federal Ministry for Education and Research within the project EFoBatt (grant number 13XP5129) is gratefully acknowledged.

## ■ ABBREVIATIONS

APTMS, 3-aminopropyltrimethoxysilane
CE, Coulombic efficiency
CEI, cathode electrolyte interphase
CV, cyclic voltammetry
EC, ethylene carbonate
EDX, energy-dispersive X-ray analysis
EIS, electrochemical impedance spectroscopy
eV, electron volt
FTIR, Fourier transform infrared spectroscopy
LIB, lithium-ion battery
NMC, $LiNi_xCo_yMn_{1-x-y}O_2$
NP, nanoparticle
OCP, open-circuit potential
OCV, open-circuit voltage
QC, quantum chemistry
SEM, scanning electron microscopy
SEI, solid electrolyte interphase
SHINERS, shell-isolated nanoparticle-enhanced Raman spectroscopy

## ■ REFERENCES

(1) Li, W.; Song, B.; Manthiram, A. High-Voltage Positive Electrode Materials for Lithium-Ion Batteries. *Chem. Soc. Rev.* **2017**, *46*, 3006−3059.
(2) Cho, Y.; Oh, P.; Cho, J. A new Type of Protective Surface Layer for High-Capacity Ni-based Cathode Materials: Nanoscaled Surface Pillaring Layer. *Nano Lett.* **2013**, *13*, 1145−1152.
(3) Wang, J.; Yamada, Y.; Sodeyama, K.; Chiang, C. H.; Tateyama, Y.; Yamada, A. Superconcentrated Electrolytes for a High-Voltage Lithium-Ion Battery. *Nat. Commun.* **2016**, *7*, 12032.
(4) Zhang, X.; Zou, L.; Xu, Y.; Cao, X.; Engelhard, M. H.; Matthews, B. E.; Zhong, L.; Wu, H.; Jia, H.; Ren, X.; et al. Advanced Electrolytes for Fast-Charging High-Voltage Lithium-Ion Batteries in Wide-Temperature Range. *Adv. Energy Mater.* **2020**, *10*, 2000368.
(5) Zhang, S.; Ma, J.; Hu, Z.; Cui, G.; Chen, L. Identifying and Addressing Critical Challenges of High-Voltage Layered Ternary Oxide Cathode Materials. *Chem. Mater.* **2019**, *31*, 6033−6065.
(6) Mohanty, D.; Dahlberg, K.; King, D. M.; David, L. A.; Sefat, A. S.; Wood, D. L.; Daniel, C.; Dhar, S.; Mahajan, V.; Lee, M.; et al. Modification of Ni-Rich FCG NMC and NCA Cathodes by Atomic Layer Deposition: Preventing Surface Phase Transitions for High-Voltage Lithium-Ion Batteries. *Sci. Rep.* **2016**, *6*, 26532.
(7) Li, X.; Liu, J.; Banis, M. N.; Lushington, A.; Li, R.; Cai, M.; Sun, X. Atomic Layer Deposition of Solid-State Electrolyte Coated Cathode Materials with Superior High-Voltage Cycling Behavior for Lithium Ion Battery Application. *Energy Environ. Sci.* **2014**, *7*, 768−778.
(8) Li, T.; Yuan, X.-Z.; Zhang, L.; Song, D.; Shi, K.; Bock, C. Degradation Mechanisms and Mitigation Strategies of Nickel-Rich NMC-Based Lithium-Ion Batteries. *Electrochem. Energy Rev.* **2020**, *3*, 43−80.
(9) Li, Q.; Wang, Y.; Wang, X.; Sun, X.; Zhang, J.-N.; Yu, X.; Li, H. Investigations on the Fundamental Process of Cathode Electrolyte Interphase Formation and Evolution of High-Voltage Cathodes. *ACS Appl. Mater. Interfaces* **2020**, *12*, 2319−2326.
(10) Fan, X.; Wang, C. High-Voltage Liquid Electrolytes for Li Batteries: Progress and Perspectives. *Chem. Soc. Rev.* **2021**, *50*, 10486−10566.
(11) Takahashi, I.; Kiuchi, H.; Ohma, A.; Fukunaga, T.; Matsubara, E. Cathode Electrolyte Interphase Formation and Electrolyte Oxidation Mechanism for Ni-Rich Cathode Materials. *J. Phys. Chem. C* **2020**, *124*, 9243−9248.
(12) Yoon, W.-S.; Nam, K.-W.; Jang, D.; Chung, K. Y.; Hanson, J.; Chen, J.-M.; Yang, X.-Q. Structural Study of the Coating Effect on the Thermal Stability of Charged MgO-Coated LiNi0.8Co0.2O2 Cathodes Investigated by In Situ XRD. *J. Power Sources* **2012**, *217*, 128−134.
(13) Song, B.; Li, W.; Oh, S.-M.; Manthiram, A. Long-Life Nickel-Rich Layered Oxide Cathodes with a Uniform Li2ZrO3 Surface Coating for Lithium-Ion Batteries. *ACS Appl. Mater. Interfaces* **2017**, *9*, 9718−9725.
(14) Park, M.-H.; Noh, M.; Lee, S.; Ko, M.; Chae, S.; Sim, S.; Choi, S.; Kim, H.; Nam, H.; Park, S.; et al. Flexible High-Energy Li-Ion Batteries with Fast-Charging Capability. *Nano Lett.* **2014**, *14*, 4083−4089.
(15) Myung, S.-T.; Izumi, K.; Komaba, S.; Sun, Y.-K.; Yashiro, H.; Kumagai, N. Role of Alumina Coating on Li−Ni−Co−Mn−O Particles as Positive Electrode Material for Lithium-Ion Batteries. *Chem. Mater.* **2005**, *17*, 3695−3704.
(16) Li, D.; Kato, Y.; Kobayakawa, K.; Noguchi, H.; Sato, Y. Preparation and Electrochemical Characteristics of LiNi1/3Mn1/3Co1/3O2 Coated with Metal Oxides Coating. *J. Power Sources* **2006**, *160*, 1342−1348.
(17) von Aspern, N.; Diddens, D.; Kobayashi, T.; Börner, M.; Stubbmann-Kazakova, O.; Kozel, V.; Röschenthaler, G.-V.; Smiatek, J.; Winter, M.; Cekic-Laskovic, I. Fluorinated Cyclic Phosphorus(III)-Based Electrolyte Additives for High Voltage Application in Lithium-Ion Batteries: Impact of Structure-Reactivity Relationships on CEI Formation and Cell Performance. *ACS Appl. Mater. Interfaces* **2019**, *11*, 16605−16618.
(18) Sun, D.; Wang, Q.; Zhou, J.; Lyu, Y.; Liu, Y.; Guo, B. Forming a Stable CEI Layer on LiNi0.5Mn1.5O4Cathode by the Synergy Effect of FEC and HDI. *J. Electrochem. Soc.* **2018**, *165*, A2032−A2036.
(19) Qian, Y.; Niehoff, P.; Börner, M.; Grützke, M.; Mönnighoff, X.; Behrends, P.; Nowak, S.; Winter, M.; Schappacher, F. M. Influence of Electrolyte Additives on the Cathode Electrolyte Interphase (CEI) Formation on LiNi1/3Mn1/3Co1/3O2 in Half Cells with Li Metal Counter Electrode. *J. Power Sources* **2016**, *329*, 31−40.
(20) Lu, W.; Zhang, J.; Xu, J.; Wu, X.; Chen, L. In Situ Visualized Cathode Electrolyte Interphase on LiCoO2 in High Voltage Cycling. *ACS Appl. Mater. Interfaces* **2017**, *9*, 19313−19318.
(21) Matsui, M.; Deguchi, S.; Kuwata, H.; Imanishi, N. In-operando FTIR Spectroscopy for Composite Electrodes of Lithium-ion Batteries. *Electrochemistry* **2015**, *83*, 874−878.
(22) Meng, Y.; Chen, G.; Shi, L.; Liu, H.; Zhang, D. Operando Fourier Transform Infrared Investigation of Cathode Electrolyte Interphase Dynamic Reversible Evolution on Li1.2Ni0.2Mn0.6O2. *ACS Appl. Mater. Interfaces* **2019**, *11*, 45108−45117.
(23) Weiling, M.; Pfeiffer, F.; Baghernejad, M. Vibrational Spectroscopy Insight into the Electrode|Electrolyte Interface/Interphase in Lithium Batteries. *Adv. Energy Mater.* **2022**, *12*, 2202504.
(24) Gajan, A.; Lecourt, C.; Torres Bautista, B. E.; Fillaud, L.; Demeaux, J.; Lucas, I. T. Solid Electrolyte Interphase Instability in Operating Lithium-Ion Batteries Unraveled by Enhanced-Raman Spectroscopy. *ACS Energy Lett.* **2021**, *6*, 1757−1763.
(25) Stancovski, V.; Badilescu, S. In Situ Raman Spectroscopic-Electrochemical Studies of Lithium-Ion Battery Materials: a Historical Overview. *J. Appl. Electrochem.* **2014**, *44*, 23−43.
(26) Hy, S.; Felix; Chen, Y.-H.; Liu, J.; Rick, J.; Hwang, B.-J. In Situ Surface Enhanced Raman Spectroscopic Studies of Solid Electrolyte

Interphase Formation in Lithium Ion Battery Electrodes. *J. Power Sources* **2014**, *256*, 324−328.
(27) Gross, T.; Giebeler, L.; Hess, C. Novel In Situ Cell for Raman Diagnostics of Lithium-Ion Batteries. *Rev. Sci. Instrum.* **2013**, *84*, 073109.
(28) Krause, A.; Tkacheva, O.; Omar, A.; Langklotz, U.; Giebeler, L.; Dörfler, S.; Fauth, F.; Mikolajick, T.; Weber, W. M. In Situ Raman Spectroscopy on Silicon Nanowire Anodes Integrated in Lithium Ion Batteries. *J. Electrochem. Soc.* **2019**, *166*, A5378−A5385.
(29) Lin, X.-D.; Uzayisenga, V.; Li, J.-F.; Fang, P.-P.; Wu, D.-Y.; Ren, B.; Tian, Z.-Q. Synthesis of ultrathin and compact Au@MnO2 nanoparticles for shell-isolated nanoparticle-enhanced Raman spectroscopy (SHINERS). *J. Raman Spectrosc.* **2012**, *43*, 40−45.
(30) Tian, X.-D.; Liu, B.-J.; Li, J.-F.; Yang, Z.-L.; Ren, B.; Tian, Z.-Q. SHINERS and plasmonic properties of Au Core SiO2 shell nanoparticles with optimal core size and shell thickness. *J. Raman Spectrosc.* **2013**, *44*, 994−998.
(31) Lee, Y.-S.; Lee, K.-S.; Sun, Y.-K.; Lee, Y. M.; Kim, D.-W. Effect of an Organic Additive on the Cycling Performance and Thermal Stability of Lithium-Ion Cells Assembled with Carbon Anode and LiNi1/3Co1/3Mn1/3O2 Cathode. *J. Power Sources* **2011**, *196*, 6997−7001.
(32) Lee, K.-S.; Sun, Y.-K.; Noh, J.; Song, K. S.; Kim, D.-W. Improvement of high voltage cycling performance and thermal stability of lithium-ion cells by use of a thiophene additive. *Electrochem. Commun.* **2009**, *11*, 1900−1903.
(33) Lin, H. B.; Huang, W. Z.; Rong, H. B.; Mai, S. W.; Hu, J. N.; Xing, L. D.; Xu, M. Q.; Li, W. S. Improving Cyclic Stability and Rate Capability of LiNi0.5Mn1.5O4 Cathode Via Protective Film and Conductive Polymer Formed from Thiophene. *J. Solid State Electrochem.* **2015**, *19*, 1123−1132.
(34) Xia, L.; Xia, Y.; Liu, Z. Thiophene Derivatives as Novel Functional Additives for High-Voltage LiCoO2 Operations in Lithium Ion Batteries. *Electrochim. Acta* **2015**, *151*, 429−436.
(35) Xing, L. Y.; Hu, M.; Tang, Q.; Wei, J. P.; Qin, X.; Zhou, Z. Improved Cyclic Performances of LiCoPO4/C Cathode Materials for High-Cell-Potential Lithium-Ion Batteries with Thiophene as an Electrolyte Additive. *Electrochim. Acta* **2012**, *59*, 172−178.
(36) Curtiss, L. A.; Redfern, P. C.; Raghavachari, K. Gaussian-4 Theory Using Reduced Order Perturbation Theory. *J. Chem. Phys.* **2007**, *127*, 124105.
(37) Li, J. F.; Tian, X. D.; Li, S. B.; Anema, J. R.; Yang, Z. L.; Ding, Y.; Wu, Y. F.; Zeng, Y. M.; Chen, Q. Z.; Ren, B.; et al. Surface Analysis Using Shell-Isolated Nanoparticle-Enhanced Raman Spectroscopy. *Nat. Protoc.* **2013**, *8*, 52−65.
(38) Frisch, M. J.; Trucks, G. W.; Schlegel, H. B.; Scuseria, G. E.; Robb, M. A.; Cheeseman, J. R.; Scalmani, G.; Barone, V.; Petersson, G. A.; Nakatsuji, H.; Li, X.; Caricato, M.; Marenich, A. V.; Bloino, J.; Janesko, B. G.; Gomperts, R.; Mennucci, B.; Hratchian, H. P.; Ortiz, J. V.; Izmaylov, A. F.; SonnenbergWilliams-Young, J. L.; Ding, F.; Lipparini, F.; Egidi, F.; Goings, J.; Peng, B.; Petrone, A.; Henderson, T.; Ranasinghe, D.; Zakrzewski, V. G.; Gao, J.; Rega, N.; Zheng, G.; Liang, W.; Hada, M.; Ehara, M.; Toyota, K.; Fukuda, R.; Hasegawa, J.; Ishida, M.; Nakajima, T.; Honda, Y.; Kitao, O.; Nakai, H.; Vreven, T.; Throssell, K.; Montgomery, J. A.; Peralta, J. E.; Ogliaro, F.; Bearpark, M. J.; Heyd, J. J.; Brothers, E. N.; Kudin, K. N.; Staroverov, V. N.; Keith, T. A.; Kobayashi, R.; Normand, J.; Raghavachari, K.; Rendell, A. P.; Burant, J. C.; Iyengar, S. S.; Tomasi, J.; Cossi, M.; Millam, J. M.; Klene, M.; Adamo, C.; Cammi, R.; Ochterski, J. W.; Martin, R. L.; Morokuma, K.; Farkas, O.; Foresman, J. B.; Fox, D. J.*Gaussian 16 Rev. B.01*, 2016.
(39) Hanwell, M. D.; Curtis, D. E.; Lonie, D. C.; Vandermeersch, T.; Zurek, E.; Hutchison, G. R. Avogadro: an Advanced Semantic Chemical Editor, Visualization, and Analysis Platform. *J. Cheminf.* **2012**, *4*, 17.
(40) Pracht, P.; Caldeweyher, E.; Ehlert, S.; Grimme, S.A Robust Non-Self-Consistent Tight-Binding Quantum Chemistry Method for large Molecules. ChemRxiv, **2019**. 10.26434/chemrxiv.8326202.v1.
(41) Pracht, P.; Bohle, F.; Grimme, S. Automated Exploration of the Low-Energy Chemical Space with Fast Quantum Chemical Methods. *Phys. Chem. Chem. Phys.* **2020**, *22*, 7169−7192.
(42) Grimme, S.; Bannwarth, C.; Shushkov, P. A Robust and Accurate Tight-Binding Quantum Chemical Method for Structures, Vibrational Frequencies, and Noncovalent Interactions of Large Molecular Systems Parametrized for All spd-Block Elements (Z = 1-86). *J. Chem. Theory Comput.* **2017**, *13*, 1989−2009.
(43) Bannwarth, C.; Ehlert, S.; Grimme, S. GFN2-xTB-An Accurate and Broadly Parametrized Self-Consistent Tight-Binding Quantum Chemical Method with Multipole Electrostatics and Density-Dependent Dispersion Contributions. *J. Chem. Theory Comput.* **2019**, *15*, 1652−1671.
(44) O'Boyle, N. M.; Banck, M.; James, C. A.; Morley, C.; Vandermeersch, T.; Hutchison, G. R. Open Babel: An Open Chemical Toolbox. *J. Cheminf.* **2011**, *3*, 33.
(45) Borodin, O.; Ren, X.; Vatamanu, J.; von Wald Cresce, A.; Knap, J.; Xu, K. Modeling Insight into Battery Electrolyte Electrochemical Stability and Interfacial Structure. *Acc. Chem. Res.* **2017**, *50*, 2886−2894.
(46) Borodin, O.; Olguin, M.; Spear, C. E.; Leiter, K. W.; Knap, J. Towards High Throughput Screening of Electrochemical Stability of Battery Electrolytes. *Nanotechnology* **2015**, *26*, 354003.
(47) Borodin, O.; Behl, W.; Jow, T. R. Oxidative Stability and Initial Decomposition Reactions of Carbonate, Sulfone, and Alkyl Phosphate-Based Electrolytes. *J. Phys. Chem. C* **2013**, *117*, 8661−8682.
(48) Hall, D. S.; Self, J.; Dahn, J. R. Dielectric Constants for Quantum Chemistry and Li-Ion Batteries: Solvent Blends of Ethylene Carbonate and Ethyl Methyl Carbonate. *J. Phys. Chem. C* **2015**, *119*, 22322−22330.
(49) Marenich, A. V.; Cramer, C. J.; Truhlar, D. G. Universal Solvation Model Based on Solute Electron Density and on a Continuum Model of the Solvent Defined by the Bulk Dielectric Constant and Atomic Surface Tensions. *J. Phys. Chem. B* **2009**, *113*, 6378−6396.
(50) Burns, J. C.; Sinha, N. N.; Jain, G.; Ye, H.; VanElzen, C. M.; Lamanna, W. M.; Xiao, A.; Scott, E.; Choi, J.; Dahn, J. R. Impedance Reducing Additives and Their Effect on Cell Performance: II. C3H9B3O6. *J. Electrochem. Soc.* **2012**, *159*, A1105.
(51) Haneke, L.; Frerichs, J. E.; Heckmann, A.; Lerner, M. M.; Akbay, T.; Ishihara, T.; Hansen, M. R.; Winter, M.; Placke, P. Editors' Choice-Mechanistic Elucidation of Anion Intercalation into Graphite from Binary-Mixed Highly Concentrated Electrolytes via Complementary 19F MAS NMR and XRD Studies. *J. Electrochem. Soc.* **2020**, *167*, 140526.
(52) Kasnatscheew, J.; Rodehorst, U.; Streipert, B.; Wiemers-Meyer, S.; Jakelski, R.; Wagner, R.; Laskovic, I.; Winter, M. Learning from Overpotentials in Lithium Ion Batteries: A Case Study on the LiNi1/3Co1/3Mn1/3O2(NCM) Cathode. *J. Electrochem. Soc.* **2016**, *163*, A2943.
(53) Kim, H.; Son, Y.; Park, C.; Lee, M.-J.; Hong, M.; Kim, J.; Lee, M.; Cho, J.; Choi, H. C. Germanium Silicon Alloy Anode Material Capable of Tunable Overpotential by Nanoscale Si Segregation. *Nano Lett.* **2015**, *15*, 4135−4142.
(54) von Aspern, N.; Grünebaum, M.; Diddens, D.; Pollard, T.; Wölke, C.; Borodin, O.; Winter, M.; Cekic-Laskovic, I. Methyl-Group Functionalization of Pyrazole-Based Additives for Advanced Lithium Ion Battery Electrolytes. *J. Power Sources* **2020**, *461*, 228159.
(55) Diddens, D.; Appiah, W. A.; Mabrouk, Y.; Heuer, A.; Vegge, T.; Bhowmik, A. Modeling the Solid Electrolyte Interphase: Machine Learning as a Game Changer? *Adv. Mater. Interfaces* **2022**, *9*, 2101734.
(56) Peljo, P.; Girault, H. H. Electrochemical potential window of battery electrolytes: the HOMO-LUMO misconception. *Energy Environ. Sci.* **2018**, *11*, 2306−2309.
(57) Delp, S. A.; Borodin, O.; Olguin, M.; Eisner, C. G.; Allen, J. L.; Jow, T. R. Importance of Reduction and Oxidation Stability of High Voltage Electrolytes and Additives. *Electrochim. Acta* **2016**, *209*, 498−510.


https://doi.org/10.1021/acsami.2c17958
*ACS Appl. Mater. Interfaces* 2023, 15, 6676−6686

(58) Schmiegel, J.-P.; Qi, X.; Klein, S.; Winkler, V.; Evertz, M.; Nölle, R.; Henschel, J.; Reiter, J.; Terborg, L.; Fan, Q.; et al. Improving the Cycling Performance of High-Voltage NMC111 || Graphite Lithium Ion Cells By an Effective Urea-Based Electrolyte Additive. *J. Electrochem. Soc.* **2019**, *166*, A2910−A2920.
(59) Meethong, N.; Kao, Y.-H.; Carter, W. C.; Chiang, Y.-M. Comparative Study of Lithium Transport Kinetics in Olivine Cathodes for Li-ion Batteries. *Chem. Mater.* **2010**, *22*, 1088−1097.
(60) Dudney, N. J. Addition of a Thin-Film Inorganic Solid Electrolyte (Lipon) as a Protective Film in Lithium Batteries with a Liquid Electrolyte. *J. Power Sources* **2000**, *89*, 176−179.
(61) Varini, M.; Ko, J. Y.; Svens, P.; Mattinen, U.; Klett, M.; Ekström, H.; Lindbergh, G. On Resistance and Capacity of LiNi1/3Mn1/3Co1/3O2 Under High Voltage Operation. *J. Energy Storage* **2020**, *31*, 101616.
(62) Matsuda, Y.; Kuwata, N.; Okawa, T.; Dorai, A.; Kamishima, O.; Kawamura, J. In situ Raman spectroscopy of Li CoO2 cathode in Li/Li3PO4/LiCoO2 all-solid-state thin-film lithium battery. *Solid State Ionics* **2019**, *335*, 7−14.
(63) Zhu, Y.; Casselman, M. D.; Li, Y.; Wei, A.; Abraham, D. P. Perfluoroalkyl-Substituted Ethylene Carbonates: Novel Electrolyte Additives for High-Voltage Lithium-Ion Batteries. *J. Power Sources* **2014**, *246*, 184−191.
(64) Wada, N.; Solin, S. A. Raman Efficiency Measurements of Graphite. *Phys. B+C* **1981**, *105*, 353−356.
(65) Nishi, T.; Nakai, H.; Kita, A. Visualization of the State-of-Charge Distribution in a LiCoO 2 Cathode by In Situ Raman Imaging. *J. Electrochem. Soc.* **2013**, *160*, A1785−A1788.
(66) Alakhras, F.; Holze, R. Redox thermodynamics, conductivity and Raman spectroscopy of electropolymerized furan-thiophene copolymers. *Electrochim. Acta* **2007**, *52*, 5896−5906.
(67) Chen, F.; Shi, G.; Zhang, J.; Fu, M. Raman Spectroscopic Studies on the Structural Changes of Electrosynthesized Polythiophene Films during the Heating and Cooling Processes. *Thin Solid Films* **2003**, *424*, 283−290.
(68) Shi, G.; Xu, J.; Fu, M. Raman Spectroscopic and Electrochemical Studies on the Doping Level Changes of Polythiophene Films during Their Electrochemical Growth Processes. *J. Phys. Chem. B* **2002**, *106*, 288−292.
(69) Karim, M. R.; Lee, C. J.; Lee, M. S. Synthesis and Characterization of Conducting Polythiophene/Carbon Nanotubes Composites. *J. Polym. Sci., Part A: Polym. Chem.* **2006**, *44*, 5283−5290.


https://doi.org/10.1021/acsami.2c17958
*ACS Appl. Mater. Interfaces* 2023, 15, 6676−6686